Angular momentum in harmonic generation and above-threshold ionization

Xiushan Chen, Anna Sanpera, and Keith Burnett
Clarendon Laboratory, Department of Physics, University of Oxford, Oxford OX1 3PU, United Kingdom
(Received 8 September 1994; revised manuscript received 14 December 1994)

In this paper, we present a discussion of the role that angular momentum plays in the interaction of an intense laser field with a single-electron atom. To do this, we have made a detailed analysis of how different partial waves, i.e., different angular-momentum states, participate in producing the photoelectron energy, angular distributions, and harmonic generation spectra. We show that the two regimes—tunneling and multiphoton excitation—correspond to quite distinct evolution patterns across the partial wave decomposition. The natures of these patterns are particularly significant in the harmonic generation spectra and emphasize how harmonic generation is mainly produced in transitions back to the initial state. We also find that at high intensities, the photoelectron energy spectrum is composed of two different but well defined sets of above-threshold ionization peaks. These two sets are separated by a structureless region and the second set deviates substantially from the initial exponential decrease of the peak intensities versus energy. Similar features have been very recently reported experimentally.

PACS number(s): 32.80.Rm, 42.50.Hz

I. INTRODUCTION

There has been a great deal of progress in recent years on the theoretical description of ionization of atoms in intense laser fields [1]. Depending on the laser field parameters, the dynamics of the atom-laser interaction admits quite distinct interpretations. There are, however, two limiting ways to describe the escape of an electron from an atom by the action of a laser field: multiphoton ionization (MPI) and tunneling ionization (TI) [2–5]. In the MPI limit, the ionization is thought of as occurring via the absorption of several photons of the field (MPI). In the case of tunneling, we think of the field acting as a quasistatic (high-intensity, low-frequency) field diminishing the atomic potential barrier and allowing the electron to escape through or over the barrier (TI). Conventionally the adiabaticity or Keldysh parameter γ is used as an indication of which of these two regimes ionization occurs in. γ is defined thus

$$\gamma = \sqrt{\frac{U_i}{2U_p}}, \tag{1}$$

where U_i is the ionization potential and $U_p = E^2/4\omega^2$ the ponderomotive potential, both expressed in atomic units. In the limiting case $\gamma \ll 1$ ($U_p \gg U_i$), we say that we are in the tunneling regime, whereas for $\gamma \gg 1$ ($U_p \ll U_i$) we say that multiphoton absorption dominates. In this paper we want to explain how angular properties can be used to extract dynamical information of the ionization process. To do that we study the angular momentum dependence of harmonic generation and the photoelectron spectrum (with an emphasis on the angular distributions) in different regimes. We shall limit our study to hydrogen [6–8], starting from the ground state and interacting with a linearly polarized field at different frequencies and intensities, corresponding to a range of γ from $\gamma = 0.55$ to $\gamma = 3$.

The paper is organized as follows. In Sec. II a general description of the theory and the method used in our calculations is presented. Section III is devoted to the angular momentum analysis of harmonic generation. In Sec. IV we deal with photoelectron spectra, explaining the different methods we use to calculate the ATI spectra; the angular distributions we obtain for the different regimes are shown in Sec. V. Finally, in Sec. VI we present the conclusions of our study.

II. THEORY AND NUMERICAL NOTES

We shall briefly outline the theory we use in our calculation before describing the role of orbital angular momentum in the production of harmonics and high-energy electrons in a multiphoton ionization process. Our approach is based on the numerical solution on a grid of the time-dependent Schrödinger equation (atomic units are used throughout)

$$i\frac{\partial}{\partial t}\psi(\vec{r},t) = (\hat{H}_0 + \hat{H}_{\rm int})\psi(\vec{r},t)\ . \tag{2}$$

For the hydrogen atom, in the dipole approximation, this can be written in the form

$$i\frac{\partial}{\partial t}\psi(\vec{r},t) = \left(-\frac{1}{2}\vec{\nabla}^2 - \frac{1}{r} + rE(t)\cos\theta\sin\omega t\right)\psi(\vec{r},t), \tag{3}$$

where $\vec{E}(t)$ is the electric field envelope. The total electronic wave function can then be expanded in an angular-momentum basis

$$\psi(\vec{r},t)=\sum_{l=0}^{\infty}\sum_{m=-l}^{m=l}\frac{1}{r}\chi_l(r,t)\,Y_l^m(\theta,\phi)\ . \tag{4}$$

Here $Y_l^m(\theta,\phi)$ are the standard spherical harmonics. If the field is linearly polarized along the z axis and the initial state is an s state, only the spherical harmonics with $m=0$ will contribute and we can eliminate the m index in the above expression. This expansion of the wave function, in which the whole time dependence is included only in the radial part, leads to a set of coupled partial differential equations.

Explicitly, for each l component of the expansion, the coupled equations are [9–11]

$$i\frac{\partial}{\partial t}\chi_l(r,t)=\left[-\frac{1}{2}\frac{\partial^2}{\partial r^2}-\frac{1}{r}+\frac{l(l+1)}{2r^2}\right]\chi_l(r,t) +rE(t)\sin\omega t\ \left[c_l^+\chi_{l+1}(r,t)+c_l^-\chi_{l-1}(r,t)\right]\ . \tag{5}$$

Here $c_l^{\pm}$ are coupling constants related to Clebsch-Gordan coefficients, having the form

$$c_l^+=c_{l+1}^-=\sqrt{\frac{(l+1)^2}{(2l+3)(2l+1)}}\ . \tag{6}$$

Each angular-momentum l state is therefore coupled by the laser field to $l\pm1$ states (except $l=0$, which is coupled only to $l=1$). The evolution of the electronic wave function in our calculation is performed using an efficient split-operator technique. The advantages of this technique are unitary evolution and numerical stability. Using a split-operator method we can write the evolution due to Eq. (5) in the approximate form [12]

$$\chi_l(r,t+\Delta t)=e^{-i\hat{H}_0\Delta t/2}e^{-i\hat{H}_{\rm int}\Delta t}e^{-i\hat{H}_0\Delta t/2}\chi_l(r,t) +O(\Delta t^3)\ , \tag{7}$$

where $\hat{H}_0$ stands for the bare Hamiltonian, and $\hat{H}_{\rm int}$ for the interaction part as written in Eq. (5). The wave function $\chi_l(r,t)$ can then be obtained numerically over successive time steps by using this operation repeatedly on the initial electronic wave function. There are several techniques in handling the split form of the evolution operator [see Eq. (7)], especially the exponential coupling operator [9–12]. We choose to diagonalize the interchannel coupling in a basis in which $\cos\theta$ is diagonal. The treatment of the interaction term is then straightforward since the exponential of a diagonal matrix is simply a matrix of the exponentials.

The box in which the simulation is done depends now on two discrete variables: the radial coordinate r and the angular momentum l. The size of the box used in the simulations is determined by physical requirements. The radial boundary has to be far enough from the nucleus in order to avoid significant reflections from the boundaries that could distort the dynamics of the process. This problem is partially solved by using an absorbing mask function of $\cos^{\frac{1}{8}}(r_{\rm max}-50.0)/100.0$ varying from 1 to 0 in the last 50 a.u. [14]. Even then, the size of the box has to be large enough to avoid the genuine ingoing parts of the wave function (produced by the laser field) being absorbed by the mask function. As a consequence of the absorbing boundary we can use the decrease of the normalization of the total wave function as a measure of ionization.

It is, of course, not possible to use an infinite number of angular momentum l states in the time evolution of the electronic wave function, so a cutoff in the expansion of l [see Eq. (4)] has to be introduced. For low intensities, when perturbation theory to the lowest order (LOPT) can be used to describe a process, dipole selection rules will effectively restrict the wave function expansion in angular momentum states. This means that if an s state requires n photons to ionize, the final state will be a mixture of all angular momentum components with $0\le l\le n$. For higher intensities, however, LOPT is no longer valid and states with higher angular momentum become *a priori* as important as the states with $l\le n$. The critical question is, of course, how many angular states are necessary to describe accurately a process for a given frequency, intensity, and pulse length. Since the different partial waves are coupled through the interaction term, it seems logical that the number of partial waves has to increase with the laser intensity. We shall see in fact that the number of angular states ($l_{\rm max}$) necessary to get reasonable convergence depends strongly on the observable we are calculating.

Spurious reflections from the edge of the "angular" box, i.e., the $l_{\rm max}$ partial wave, can be avoided by using an absorber. In some cases, the use of an angular absorber has allowed us to reduce the number of partial waves by a factor of 2. The angular absorber, when used, is included over the last six to ten partial waves. This is especially important in analyzing the photoelectron spectra for high intensities, as we shall see in the following sections.

To summarize, the size of the box ranges between 300 and 900 a.u. with a radial absorber mask function in the last 50 a.u. The spatial step is $0.10\le\Delta r\le0.25$ a.u. [small spatial steps are required if the number of above-threshold ionization (ATI) peaks in the spectrum extends to high orders] and the temporal step varies between 512 and 2048 steps per optical cycle. (The smaller spatial and temporal steps are usually needed to see any improvement of the spectrum.) The cutoff in the angular expansion in most of the cases varies as $12\le l_{\rm max}\le96$, with $l_{\rm max}$ increasing until convergence is achieved.

III. HARMONIC GENERATION

A. Acceleration and angular decomposition

The radiation emitted by a single charge (harmonic emission) in an external field is determined by its acceleration [15]. Many calculations of the harmonic generation, however, are based on finding the Fourier transformation of the dipole moment. However, for high intensities and hence rapid ionization, the dipole moment and its velocity do not vanish at the end of the pulse and can give

an unphysical contribution to the spectrum. The acceleration form therefore seems the most reliable method to compute harmonic emission and this is the expression we use:

$$P(\omega) \propto \left| \int_0^T \ddot{d}(t)\, e^{-i\omega t}\, dt \right|^2 . \tag{8}$$

Here T is the duration of the laser pulse and $\ddot{d}(t)$ is the acceleration. With the help of Ehrenfest's theorem, the dipole acceleration can be expressed in the form

$$\begin{aligned} \ddot{d}(t) &= \frac{d^2}{dt^2} \langle \Psi(\vec{r},t)\, |z|\, \Psi(\vec{r},t) \rangle \\ &= -\left\langle \Psi(\vec{r},t) \left| \frac{\partial}{\partial z} [V(r) + H_{\rm int}] \right| \Psi(\vec{r},t) \right\rangle . \end{aligned} \tag{9}$$

Introducing the angular decomposition of the wave function in Eq. (9), we find

$$\begin{aligned} \ddot{d}(t) &= \sum_l \ddot{d}_l(t) + E(t) \sin\omega t \\ &= -\sum_{l=0}^{l_{\max}-1} C_l^+ \left(\left\langle \chi_l(r,t) \left| \frac{1}{r^2} \right| \chi_{l+1}(r,t) \right\rangle \right. \\ &\quad \left. + \left\langle \chi_{l+1}(r,t) \left| \frac{1}{r^2} \right| \chi_l(r,t) \right\rangle \right) \\ &\quad + E(t) \sin\omega t . \end{aligned} \tag{10}$$

The first pair of terms in (10) corresponds to all the possible dipole transitions ($\Delta l = \pm 1$) between different angular states. The last term is simply the quiver acceleration of the external field at the incident frequency. It is clear from (8), that it is meaningless to calculate the transition between l and $l+1$ separately since the spectrum is proportional to the square of the absolute value of the Fourier transformation of Eq. (10). These separate contributions, however, do give us some important insight into the role of angular momentum in the harmonic generation process [16]. For this reason we shall discuss the spectra produced by each contribution

$$P_l(\omega) \propto \left| \int_0^T [\ddot{d}_l(t) + E(t) \sin\omega t]\, e^{-i\omega t}\, dt \right|^2 . \tag{11}$$

The $E(t)\sin\omega t$ term is included in each dipole transition merely to generate the fundamental peak. We call these different components $P_l(\omega)$ partial dipole contributions.

B. Convergence in terms of partial waves

To ensure a good contrast in ionization mechanisms, we shall consider two very different cases. For the first the laser frequency is $\omega_1 = 0.2$ a.u. (5.4 eV) and the intensity is $I_1 = 1.7 \times 10^{14}$ W/cm^2, which corresponds to a high-frequency ionization regime (nominally a three-photon process) with the Keldysh parameter $\gamma_1 = 2.8$. We shall refer to it as the high-frequency–MPI case. The second case corresponds to a low-frequency regime with a frequency $\omega_2 = 0.042$ a.u. (1.14 eV) and intensity $I_2 = 8.8 \times 10^{13}$ W/cm^2 (now $\gamma = 0.84$). We shall refer to this as the low-frequency–TI case. The two labels "MPI" and "TI" should be regarded only as an indication of the dominant ionization mechanism for these frequencies and intensities. For both cases the pulses used have a sine^2 profile and are 96 optical cycles long.

First we analyze the convergence of the harmonic spectra in terms of the $l_{\max}$ cutoff. We observe that the number of partial waves necessary to get convergence is relatively low for both the high and the low-frequency regimes [17]. Figures 1 and 2 show the harmonic emission convergence for the high- and the low-frequency cases, respectively. In Fig. 1 we show the harmonic spectrum (the relevant part of it) obtained with $l_{\max} = 12$ [Fig. 1(a)] and with $l_{\max} = 24$ [Fig. 1(b)]. For the low-frequency case we find that the convergence of the harmonic spectrum requires more partial waves than that of the high-frequency case. This can be seen in Fig. 2, where the total harmonic spectra with $l_{\max} = 24$ [Fig. 2(a)], and $l_{\max} = 48$ [Fig. 2(b)] are shown. For this case at least 24 partial waves are needed to obtain convergence. The relatively small changes between Figs. 1(a) and 1(b) and between Figs. 2(a) and 2(b) indicate the degree of convergence achieved.

Insight into the role of different partial waves can be obtained through analysis of the partial dipole contributions as defined in Eq. (11). Figure 3 shows the partial wave contributions, in the MPI case, for the transitions between $l = 0,1$, $l = 1,2$, and $l = 4,5$ states as labeled in the figure, together with the total spectrum. We see in Fig. 3 that the $l = 0,1$ partial contribution describes accurately the total harmonic spectrum inside the $U_i + 3U_p$ plateau region, i.e., up to the third harmonic (in fact, up to the seventh harmonics is well produced by the $l = 0,1$ transition). This reinforces the notion that

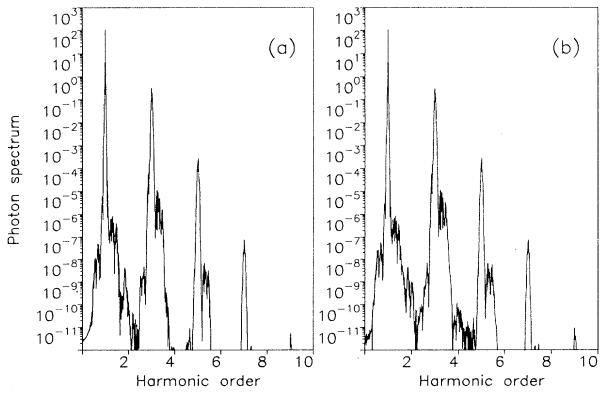

FIG. 1. Angular convergence in the harmonic generation spectrum for high frequency (only the relevant part of the spectrum is shown). The calculations are done for a 96-cycle pulse with peak laser intensity $I_1 = 1.7 \times 10^{14}$ W/cm^2 and $\omega = 0.2$ a.u. (5.4 eV) with (a) $l_{\max} = 12$ and (b) $l_{\max} = 24$.

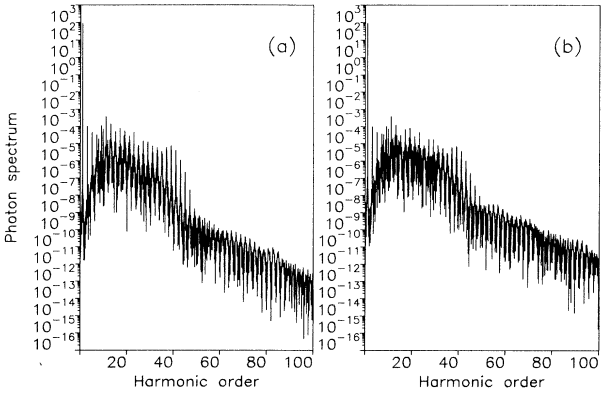

FIG. 2. Angular convergence in the harmonic generation spectrum for low frequency with (a) $l_{max} = 24$ and (b) $l_{max} = 48$ at peak laser intensity $I_2 = 8.8 \times 10^{13}$ W/cm^2 and $\omega = 0.042$ a.u. (1.14 eV).

harmonic emission is dominated by transitions ending in the ground state ($l = 0$). This notion is further backed up by the observation of a large number of very weak components outside the plateau region (see Fig. 4). These high-order low-intensity harmonic components, in spite of being very small indeed, are well above the total harmonic spectrum background and eventually die away for transitions between higher l states. This is presumably because they do not come from transitions back to the ground state. These high-order low-intensity harmonics make no discernible contribution to the total spectrum due to interferences between different partial contributions. They are, in any case, of no practical importance since they occur well outside the plateau region where efficient generation occurs. Figure 5 shows the partial contributions in the low-frequency case. The $l = 0, 1$ partial contribution for this case contains virtually all of the total harmonic spectrum, the plateau, and the cutoff and, furthermore, the other higher l contributions are well below the total harmonic background.

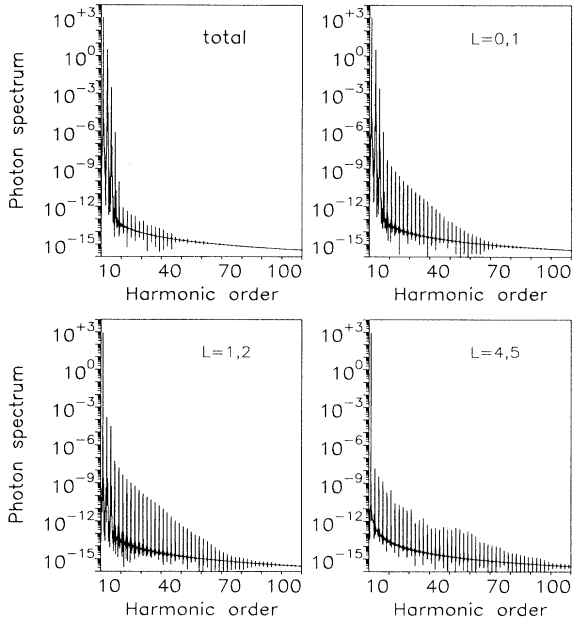

FIG. 4. Same as Fig. 3, but now showing the complete harmonic spectrum and some dipole contributions. We can observe a large number of weak harmonic components outside the plateau region that appear in the different dipole partial contributions. This high-l-order components do not appear in the total spectrum due to the interferences between different partial contributions.

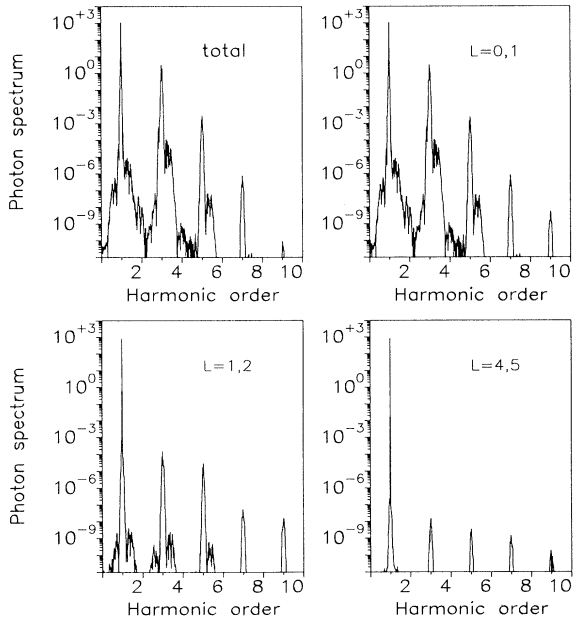

FIG. 3. Harmonic partial dipole contributions for the relevant part of the harmonic spectrum at $\omega = 0.2$ a.u. The first plot (total) is simply Fig. 1(a), which has been included for the sake of comparison with the partial contributions. The other plots correspond to the dipole transitions $l = 0, 1$; $l = 1, 2$; and $l = 4, 5$, respectively. The laser field parameters are the same as in Fig. 1.

Thus we have found that for both the high- and the low-frequency cases, the harmonic spectrum inside the plateau is reproduced by the $l = 0 \leftrightarrow l = 1$ transition. In fact, the "alternate" dipole form [13,14] shows that the sources of the high-order harmonics are transitions that are dipole connected to the ground state. Our result confirms the idea that harmonic emission is dominated by transitions ending in the ground state ($l = 0$ state). For the MPI case, there are clear but rather small (insignificant experimentally) contributions from high l transitions that do not contribute to the total spectrum. These high l contributions do show, however, that a small part of the wave packet reaches quite high l states. In the low-frequency case, in contrast, the partial contributions for $l > 1$ never extend to higher orders than the $l = 1$ contribution and are always below the total harmonic background. We now want to discuss why the total convergence—in terms of the number of angular states—is slower for the low-frequency case (TI) than for the

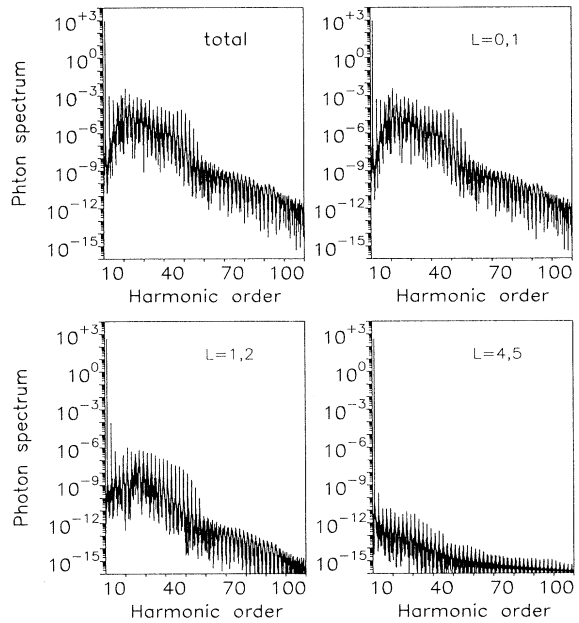

FIG. 5. Same as Fig. 4, but now for the low-frequency $\omega = 0.042$ case. The $l = 0, 1$ partial contribution reproduces well the total harmonic spectrum also outside the plateau region. All the other partial contributions are well below the total harmonic background.

higher-frequency case (MPI). The differences between the two regimes in the $l_{\max}$ convergence arise from the very distinct dynamical evolution of the respective wave packets. We can see why such a distinction is to be expected in the following way. In the low-frequency case where tunneling ionization dominates, we expect the harmonic generation to be produced by a part of the wave packet that has tunneled through the barrier and then returned back to the core. To describe this piece of wave packet, displaced from the core (and orientated in the direction of the laser field), oscillating in a nearly classical fashion, will require a large number of l states. One should think of a wave packet with a quite small initial extent ($\simeq$ 1 a.u.) and an oscillation amplitude $\alpha \simeq E/\omega^2$, i.e., the classical excursion parameter. This wave packet has, at the extreme of the oscillation, i.e., $r \simeq \alpha$, an angular spread of the order of $1/\alpha$ and therefore must contain a number $l \simeq \alpha$ of partial waves. Truncating the $l_{\max}$ expansion with a low l number would therefore cause the loss of angular resolution of the wave packet when it is displaced from the core. Subsequent evolution of this excited wave packet then would not be accurately represented, especially the recollision that produces harmonics at the core. In the MPI regime, in contrast, many high l angular states are excited during the ionization process that do not contribute appreciably to the harmonic spectrum. The MPI does have, as we have seen, small components in the partial contributions at high l. These small components, however, do not influence the total harmonic spectrum. The harmonic emission is mainly produced by the s and the p components of the excited (continuum) wave packet that remains close to the nucleus and therefore the time evolution of higher ($l \gg 1$) states, which do not return to the nucleus, does not affect the harmonic emission.

IV. PHOTOELECTRON SPECTRUM

In this section we present our results concerning the photoelectron spectrum in the low- and the high-frequency domains. At moderate or relatively high intensities we expect to find the spectra composed of a set of peaks separated by the energy of one laser photon with an overall exponential decrease with energy. This well known structure is commonly referred to as an ATI spectrum. We observe that the peak structure holds even for very high intensities, but certainly not with an exponential decrease in energy. As in Sec. III, we shall first address in detail the number of partial waves needed to obtain convergence for various cases. The technical issues related to the methods we use to compute the ATI spectra are addressed mainly in the Appendix, although we briefly review our method in the following subsection.

A. Method

The method we use to calculate the photoelectron spectra is based on the projection of the final wave function $\Psi(\vec{r}, t = T)$ onto wave functions for the continuum, i.e., scattering states. We have checked this method against two other methods, namely, the window operator method [18] and finally an asymptotic transformation to momentum space. All of those methods rely on the complete knowledge of the electronic wave function at the end of the pulse. For all the calculations we present here, the normalization at the end of the pulse $\Psi(\vec{r}, t = T)$ is always very close to one. This is accomplished by using very short pulses (8 or 14 cycles long), which allows us to obtain the ATI spectra for very high-intensity lasers but using reasonable numerical grids. To ensure the accuracy of our results we also calculate the radial distribution of the final wave function through a wavelet analysis or R profile [19]. We discard the peaks in which there is a significant contribution from the wave packet that has already been absorbed by the mask function at the end of the box. As an example, in Fig. 6 we present a comparison between the three different methods: (a) projection, (b) the window operator, and (c) a Fourier transformation to momentum space. The projection method is apparently able to solve the spectrum up to higher orders. However, after the R profile, we observe that high-order peaks after the ninth have important missing parts that have propagated to the boundary and therefore they must not be considered.

B. Convergence in terms of partial waves

In contrast to harmonic generation, the number of partial waves needed to converge the photoelectron spectrum varies greatly with the laser intensity. This is especially

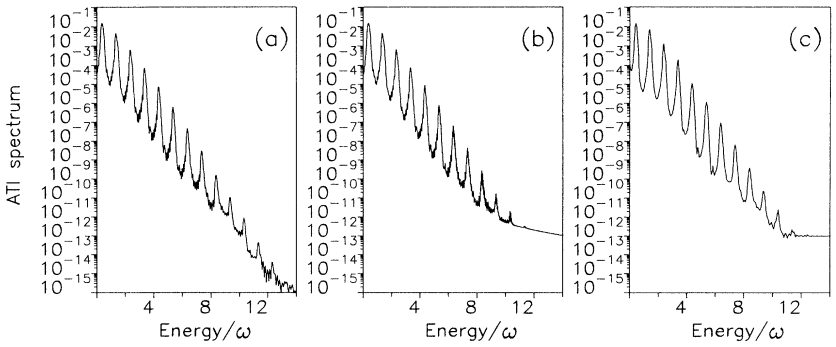

FIG. 6. Comparison between the photoelectron spectra calculated using three different methods: (a) projection method, (b) window operator method, and (c) Fourier transformation to momentum space. The laser parameters are $I_1 = 1.7 \times 10^{14}$ W/cm^2, $\omega = 0.2$ a.u. for a 14-cycle pulse with a linear turn-on and turn-off of two cycles. The total number of angular states in the wave function expansion is $l_{\max} = 12$.

clear for low values of the Keldysh parameter and therefore it is more drastic in the low-frequency domain and/or very high laser intensities, where we observe that a large number of partial waves are important in forming the spectrum.

Our results are presented in Figs. 7–9. For the high-frequency case and moderate intensities (e.g., $I = 1.7 \times 10^{14}$ W/cm^2) but large Keldysh parameter ($\gamma = 2.8$), convergence is rapidly achieved. This can be seen in Fig. 7, where the ATI spectrum is displayed using (a) $l_{\max} = 12$ and (b) $l_{\max} = 48$. The analysis of the partial wave contributions $P_l(E)$ [see the Appendix, Eq. (16)] indicates that in this regime (large Keldysh parameter) the overall ATI spectrum is qualitatively (not quantitatively) reproduced by the s ($l = 0$) and the p ($l = 1$) contributions alone (see Fig. 8). For this case very few photons are required to reach the continuum. The propensity rule that favors transitions increasing the angular momentum ($\Delta l = +1$ instead $\Delta l = -1$) do not apply when so few photons are absorbed. In fact, we find that all the peaks (odd and even) are reproduced with just the first partial waves. The angular distributions of individual ATI peaks, however, needs many more partial waves. In fact, for this regime we observe that the angular distribution related to each s ATI peak requires $n + s$ partial contributions, as we would expect in this regime, where n is the minimum number of photons at threshold.

The convergence for the low-frequency case ($\omega_2 = 0.042$ a.u.) at moderate intensities, e.g., $I = 7.7 \times 10^{13}$ W/cm^2 and Keldysh parameter $\gamma = 0.90$, requires a large number of partial waves. Figure 9 shows the ATI spectra using (a) $l_{\max} = 48$ and (b) $l_{\max} = 96$. (In both cases an angular mask function over the last six partial waves has been used to reduce the background.) As we can see by comparing Figs. 9(a) and 9(b), the degree of convergence achieved with $l_{\max} = 48$ is still inadequate, although the major features of the spectrum are already present. After the R profile we observe that only the region corresponding to energies below 20 times the photon energy are properly resolved.

C. Different features in high-intensity ATI

Different features on the ATI spectrum have been reported [20–22] that deviate substantially from the "typical" electron energy spectrum. Instead of the expected series of peaks separated by the energy of the laser photon (expected in the multiphoton picture) with an exponential decrease of their relative intensities versus energy or the absence of a definite structure when the intensity increases, approaching the tunneling picture, a so-called

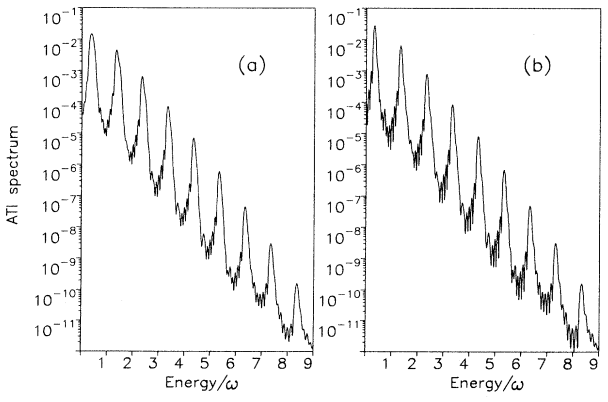

FIG. 7. Angular convergence in the ATI spectrum for the high-frequency case. Total ATI spectrum is calculated using (a) 12 and (b) 48 partial waves for a laser intensity $I_1 = 1.7 \times 10^{14}$ W/cm^2, frequency $\omega = 0.2$ a.u., and Keldysh parameter $\gamma = 2.8$

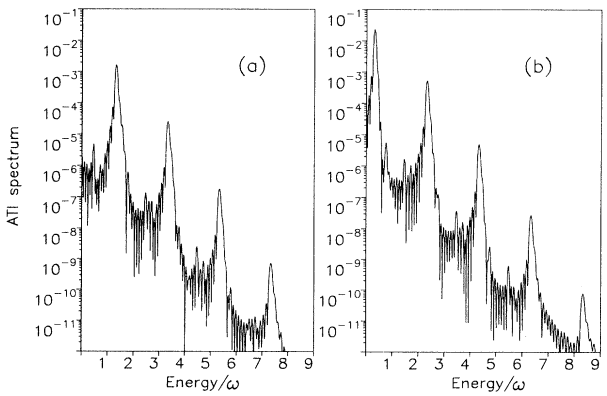

FIG. 8. (a) Partial ATI angular contribution from s states ($l = 0$) to the total ATI spectrum of Fig. 7 and (b) partial ATI angular contribution from p states ($l = 1$).

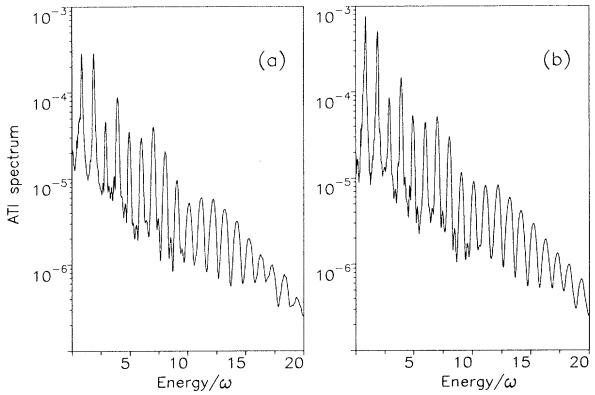

FIG. 9. Total photoelectron spectrum for $\omega = 0.042$ a.u., $I = 7.7 \times 10^{13}$ W/cm^2, and Keldysh parameter $\gamma = 0.90$ using (a) $l_{\max} = 48$ and (b) $l_{\max} = 96$.

plateau in the ATI structure has been found at high intensities [21]. Although we do not see any clear plateau in the ATI spectrum for the cases we have studied, we do find features that agree reasonably with the results from recent experiments.

To study the transition from multiphoton to tunneling, we calculate the photoelectron spectra for a wide range of intensities in both the high- and the low-frequency regimes. By doing that we scan over a large range of Keldysh parameter values, so we are really using the Keldysh parameter as an indicator of the dominant ionization description. For the high-frequency case ($\omega_1 = 0.2$ a.u.), the intensities we use range between 1.7×10^{14} and 1.7×10^{15} W/cm^2 ($2.8 \leq \gamma \leq 1$), whereas for the low-frequency case ($\omega_2 = 0.042$ a.u.), the intensities range between 2×10^{13} and 7.7×10^{13} W/cm^2 ($1.75 \leq \gamma \leq 0.90$).

We observe that for the high-frequency case, the ATI spectrum behaves as expected until intensities $I \sim 6 \times 10^{14}$ W/cm^2 ($\gamma \sim 1.5$). The ATI peaks in this region are well defined and show a clear exponential decrease in intensity with energy. At intensities around 3.5×10^{14} W/cm^2 peak suppression appears and the second ATI peak becomes the largest peak in the spectrum. Higher intensities result in very rapid ionization: the electron then has a great probability of emerging after absorbing $n + s$ photons and eventually going over a channel closing (peak suppression). The total number of ATI peaks increases and the slope of the envelope of the heights of the ATI peaks decreases when the laser intensity increases. At laser intensities around 9×10^{14} W/cm^2, $\gamma = 1.2$, the "typical" behavior breaks down and the background of the ATI spectrum increases notably. A different feature then appears: the ATI spectrum is now composed of two distinct set of peaks. In the first set, corresponding to the low-energy part of the spectrum, the peaks are not as well defined as they are for lower intensities. Stark shifted resonances appear to produce extra structures and eventually to greatly increase the background. The ATI structure is then almost smeared out after some peaks; however, a different set of very well defined ATI peaks emerges in the higher-energy range of the spectrum. Increasing further the laser intensity (e.g., 1.4×10^{15} W/cm^2), the ATI structure splits completely into two sets separated by an almost structureless region. The latter set does not follow the former exponential decrease in energy and deviates substantially from it. This can be seen as a change in the slope of the background compared to the previous part of the spectrum. These results are presented in Fig. 10 for intensities 6×10^{14}, 9×10^{14}, and 1.4×10^{15} W/cm^2 ($\gamma = 1.5$, 1.2, and 1), respectively.

Surprisingly enough, in the low-frequency case, the photoelectron spectrum presents a well defined structure even for values of the Keldysh parameter well below unity. This is not what we would have *a priori* guessed, because we expect the low-frequency dynamics to be closer to the tunneling picture than the high-frequency dynamics. Although the ionization at the end of these short pulses is, in both low- and high-frequency cases, extremely low, the ground state depletion behaves very differently in each regime. For instance, in the high-frequency case, the intensity is high enough to deplete the ground stated considerably during the turn-on of the pulse, i.e., ionization occurs at different intensities. The background increases greatly because ionization then occurs from different stages. In the low-frequency case, however, the ground state does not deplete considerably during the turn-on. Therefore the spectrum for the low-frequency case is composed of well defined ATI peaks corresponding to ionization from the ground state during the flat part of the pulse, i.e., the constant intensity. The departure from the standard ATI spectrum in the low-frequency case emerges in a different way. Again, for low intensities (a few times 10^{13} W/cm^2) the spectrum shows an exponential decrease of the peaks intensity versus energy. Increasing the intensity (see Fig. 9, where $I = 7.7 \times 10^{13}$ W/cm^2 and $\gamma = 0.90$), the photoelectron spectrum still shows very well defined peaks separated

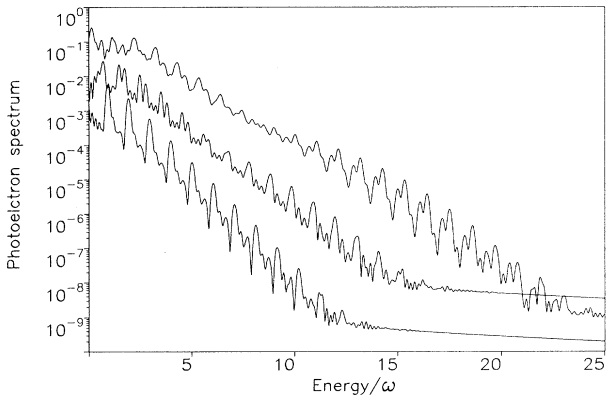

FIG. 10. Total photoelectron spectrum for the high-frequency case ($\omega = 0.2$ a.u.) and short pulse (eight cycles) at three different laser intensities. The lower curve corresponds to $I = 6 \times 10^{14}$ W/cm^2 ($\gamma = 1.5$). The middle curve corresponds to $I = 9 \times 10^{14}$ W/cm^2 ($\gamma = 1.2$) and we have multiplied the corresponding data by a factor of 10^1 for visual convenience. The upper curve corresponds to $I = 1.4 \times 10^{15}$ W/cm^2 ($\gamma = 1$). (The corresponding data have also been multiplied by a factor of 10^2 for a clear comparison.)

by the energy of a laser photon, although the shape of the ATI spectrum can no longer be considered standard. A further analysis of these effects will be presented elsewhere [23].

V. ANGULAR DISTRIBUTIONS

A. Technical aspects

For a linearly polarized laser field, the angular distribution depends only on Θ, the angle between the laser polarization and the direction of the ejected photoelectron. The calculation of angular distributions in the projection approach requires the knowledge of the asymptotic behavior of the continuum wave function. For hydrogen, the final wave function in the continuum can be written as [24]

$$|\alpha_f\rangle = 4\pi \sum_{l=0}^{\infty} i^l e^{-i\eta_l} \frac{\chi_l^c(E,r)}{r} Y_l(\theta) Y_l^*(\Theta) \ , \tag{12}$$

where the subscript f stands for the final continuum wave function. Here $\chi_l^c(E,r)$ is the radial part after partial wave decomposition and η_l is the phase shift of each partial wave

$$\eta_l = \arg\Gamma\left(l+1-\frac{i}{k}\right) \ , \tag{13}$$

where k is the final electron momentum.

To obtain the angular distribution of the ejected photoelectron at some fixed energy, we simply project our final wave function $\chi(r, t=T)$ onto all the possible continuum $|\alpha_f\rangle$ final states. After integrating over the radial coordinate and summing over all the angular-momentum states, the final expression for angular distribution of the ionized photoelectron can be written as

$$P(\Theta) = \left| \sum_{l=0}^{\infty} i^l \exp\left(-i \sum_{l'=1}^{l} \arctan(-1/kl')\right) Y_l(\Theta) \int \chi_l^c(E,r) \chi_l(r, t=T)\, dr \right|^2 . \tag{14}$$

Here a recursion relation has been used to calculate the phase shift of the different angular-momentum l states. The angular distribution for a given energy range (corresponding to an ATI peak) can then be obtained by summing over a few adjacent energy bins.

B. Results

In analyzing the convergence of the angular distributions, we find that we need roughly the same (or sometimes slightly higher) number of partial waves as we need to obtain the corresponding convergent photoelectron spectrum. The angular distributions related to each of the ATI peaks in the MPI regime (see Fig. 7) are presented in Fig. 11 using $l_{\max} = 12$, 24, and 48 angular states. The differences between $l_{\max} = 12$ and $l_{\max} = 48$ are larger for the lower-order ATI peaks. This is mainly due to poorer resolution in the ATI peak positions for $l_{\max} = 12$, as shown in Fig. 7. The number of partial waves required in this regime is closely related to the number of photons absorbed (e.g., the angular distribution for the s=1 ATI peak, corresponding to the four-photon process, is dominated by $l = 0, 2, 4$ states). All the contributions from other l states contain almost no contributions, as observed by Schafer and Kulander [18].

In the low-frequency regime, we observe, as expected, that the angular distributions for higher s ATI peaks become increasingly peaked along the laser polarization direction since the propensity rule, $\delta l = +1$ in the dipole transition, favors high $l+1$ angular states after the electron absorbs an additional photon. The contribution from higher angular momentum becomes increasingly important and contributions for lower l states gradually cancel each other so that the side lobes eventually vanish. In Fig. 12 we present the angular distributions related to each of the ATI peaks shown in Fig. 9 (from $s = 0$ to $s = 15$). The overall angular distributions for the ATI peaks have two dominant lobes along the laser polarization direction and they are much narrower than the

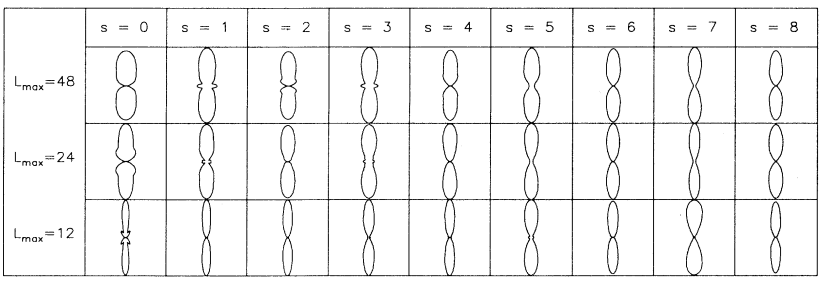

FIG. 11. Angular distributions for the ATI peaks in the MPI regime (see Fig. 7) using $l_{\max} = 48$, 24, and 12.

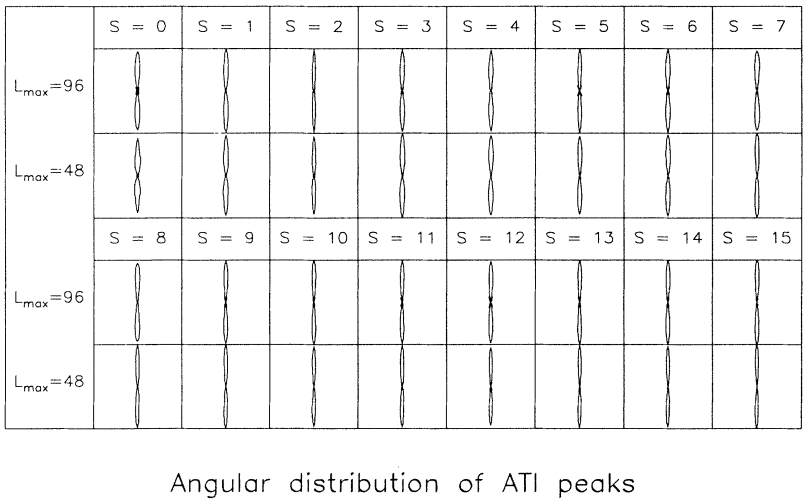

FIG. 12. Angular distributions for the ATI peaks in the low-frequency case (see Fig. 9) from $s = 0$ to $s = 15$, using $l_{max} = 48$ and 96.

peaks encountered in the high-frequency case. However, we observe that the angular distribution of some peaks presents a structure. In particular, the peaks corresponding to $s = 5 - 6$ and $s = 9 - 13$ have visible, tiny side lobes. It is for those peaks that a change in the ATI's slope becomes clear, as can be seen in Fig. 9. This agrees with the experiments performed recently by Paulus *et al.* [22], where strong narrow rings appeared in the region where the plateau in the ATI begins.

VI. CONCLUSIONS

In this paper we have examined the role of angular momentum in the high-intensity laser-atom interaction, through numerical simulations in hydrogen, emphasizing the differences between high- and low-frequency ionization regimes. We have shown that in both multiphoton and tunneling regimes, the number of partial waves that play a significant role in the harmonic emission is relatively low. This is because the efficient harmonic generation (plateau) comes from transitions ending in the initial state (ground state). Therefore, a proper description of harmonic generation requires a complete knowledge of the $l = 0$ and the $l = 1$ states along the whole pulse. For a dominant multiphoton regime this is indeed achieved with very few partial waves. Yet when tunneling dominates, a further description of the dynamic evolution of the wave packet that tunnels out and then recollides is needed and thus a larger number of partial waves has to be considered.

In contrast to harmonic generation, the electron energy spectrum has equally important contributions from a large number of partial waves and this is more evident for low-frequencies and/or high intensities, as one should expect. At high intensities we have obtained ATI spectra that substantially deviate from the typical ATI spectrum either using low or high frequencies. The different features appear as the Keldysh parameter approaches unity and are clearer for the higher-frequency case. Thus, at high frequencies and high intensities we have observed that the ATI spectrum has two distinct sets of ATI peaks that are separated by a structureless region. We have also noticed that there is a significant change in the relative slope (the intensity of the peaks versus energy) of these two sets of ATI peaks and this change becomes more evident as the intensity of the laser increases. These feature have been reported recently in experiments. At moderate intensities ($I = 7.7\times10^{13}$ W/cm^2) but low-frequencies we have found that the photoelectron spectra present very well defined ATI peaks even for values of the Keldysh parameter well below unity, but the intensity of the peaks no longer shows an exponential decrease with intensity, as shown for low intensities.

Finally, we have presented the ATI angular distributions found at high intensities and both high and low-frequencies. We have shown that the overall angular distribution for the low-frequency case is more strongly peaked along the polarization axis than in the high-frequency case. Although we have not found strong pronounced side lobes showing the emission of high-energy electrons off the polarization axis, we have seen tiny side lobes around $\theta \sim \pi/4$. These side lobes appear for those ATI peaks in which the spectrum deviates from the initial exponential decrease of the peaks' intensity with energy.

ACKNOWLEDGMENTS

We wish to thank F.H. Mies, E. Charron, and K.J. Schafer for enlightening discussions. We should also like to thank the U.K. Engineering and Physical Sciences Research Council as well as the Human and Capital Mobility program of the European Community for support. A.S. would like to thank Fleming/MEC program for financial support.

APPENDIX

1. Projection method

The energy spectrum can be obtained at the end of the pulse by projecting the evolved final wave function

$\Psi(\vec{r}, t = T)$ onto the continuum field-free wave functions. The radial eigenfunctions for a specific given energy E and orbital angular momentum l are obtained from the time-independent Shrödinger equation

$$\left\{-\frac{1}{2}\frac{\partial^2}{\partial r^2} - \frac{1}{r} + \frac{l(l+1)}{2r^2} - E\right\}\chi_l^c(E,r) = 0 \ , \qquad \text{(A1)}$$

with the initial boundary condition $\chi_l^c = 0$ at the $r = 0$. The continuum wave functions $\chi_l^c(r)$ are box normalized. The direct integration of the time-independent Schrödinger equation is straightforward. The probability to find an electron in a continuum state with an angular momentum l and energy between E and $E + dE$ is found from the projection

$$P_l(E, t = T) = \left| \int_0^{R_{\max}} \chi_l^c(E,r)\chi_l(r, t = T)dr \right|^2 \rho(E) \ , \qquad \text{(A2)}$$

where $\chi_l(r, t = T)$ is the final time evolved electronic wave function and $\rho(E)$ is the density of continuum states. $P_l(E)$ is then the partial angular ATI contribution. (Notice that, strictly speaking, the projection of the wave function onto the continuum wave functions could be done at any time at which the electric field is zero. However, if we do the projection at the early stages of the laser-atom interaction, the spectrum has not had enough time to develop and therefore well defined structures will not be found.) The projection is done for any given positive energy E and orbital momentum l above the ionization threshold of interest. The total ATI spectrum is obtained by adding all the partial angular contributions $P_l(E, t)$

$$P(E,T) = \sum_{l=0}^{l_{\max}} P_l(E,T) \ . \qquad \text{(A3)}$$

Notice that in this method we do not need to store any continuum wave function because the projection is done immediately after each continuum wave function has been generated. We calculate up to 2000 continuum wave functions for each angular momentum l to cover the range of positive energies of interest, i.e., a few atomic units of energy.

2. Fourier transformation method

An alternative method that we have used to calculate the ATI spectrum consists of a transformation from position to momentum space of the final evolved wave function. The simplest way to do it is to multiply the wave function $|\psi(\vec{r}, t = T)\rangle$ by a window function ($\sin^2$) at the end of the laser pulse before taking a spatial Fourier transform. An advantage of the Fourier transform method is that one can see the electron ATI spectrum in the momentum space and then extract information about the incoming and outgoing parts of the wave function. For the higher ATI peaks, corresponding to the most energetic photoelectrons, only outgoing parts of the wave function should contribute, but for lowest peaks, just above threshold, the ingoing part of the wave functions can be significant and that contribution should then be extracted from the ATI spectrum. From the results we have obtained for the photoelectron spectrum in momentum space, we have found that the ATI spectra are almost exclusively composed of the contributions from the outgoing ionizing wave function. The contribution from the ingoing parts of wave function is more than seven order of magnitudes lower and is indistinguishable from that from the background.

[1] For reviews on above-threshold ionization; see P. Agostini and G. Petite, Contemp. Phys. **29**, 57 (1988); J.H. Eberly, J. Javanainen, and K. Rzazewski, Phys. Rep. **204**, 331 (1991); see papers in J. Opt. Soc. Am. B **7** (1990), special issue on high-order harmonic generation, edited by K.C. Kulander and A. L'Huillier; see also reviews by a number of different authors in *Atoms in Intense Laser Fields*, edited by M. Gavrila (Academic, Boston, 1992).

[2] L.V. Keldysh, Zh. Eksp. Teor. Fiz. **47**, 1544 (1964) [Sov. Phys. JETP **20**, 1037 (1965)].

[3] S. August, D.D. Meyerhofer, D. Strickland, and S.L. Chin, J. Opt. Soc. Am B **8**, 858 (1991).

[4] E. Mevel, P. Breger, R. Trainham, G. Petite, and P. Agostini, Phys. Rev. Lett **70**, 406 (1993).

[5] P.B. Corkum, Phys. Rev. Lett. **71**, 1994 (1993).

[6] B. Wolff, H. Rottke, D. Feldmann, and K.H. Welge, Z. Phys. D **10**, 35 (1988).

[7] H. Rottke, B. Wolff, M. Brickwedde, D. Feldmann, and K.H. Welge, Phys. Rev. Lett. **64**, 404 (1990).

[8] H. Rottke, B. Wolff-Rottke, D. Feldmann, K.H. Welge, M. Dörr, R.M. Potvliege, and R. Shakeshaft, Phys. Rev. A **49**, 4837 (1994).

[9] P.L. DeVries, J. Opt. Soc. Am. **7**, 517 (1990).

[10] K.J. LaGattuta, J. Opt. Soc. Am. **7**, 639 (1990).

[11] L. Roso-Franco, A. Sanpera, M.L. Pons, and L. Plaja, Phys. Rev. A **44**, 4652 (1991).

[12] M.R. Hermann and J.A. Fleck, Jr., Phys. Rev. A **38**, 6000 (1988).

[13] J.H. Eberly, Q. Su, and J. Javanainen, J. Opt. Soc. Am. B **6**, 1289 (1989).

[14] J.L. Krause, K.J. Schafer, and K.C. Kulander, Phys. Rev. A **45**, 4998 (1992).

[15] K. Burnett, V.C. Reed, J. Cooper, and P.L. Knight, Phys. Rev. A **45**, 3347 (1992).

[16] L. Plaja and L. Roso, *Super-Intense Laser-Atom Physics*, edited by B. Piraux, A. L'Huillier, and K. Rzazewski (Plenum, New York, 1993), Vol. B316, p. 53.

[17] S.C. Rae, X. Chen, and K. Burnett, Phys. Rev. A **50**, R1946 (1994).

[18] K.J. Schafer and K.C. Kulander, Phys. Rev. A **42**, 5794 (1990).
[19] *Wavelets*, edited by J.M. Combes, A. Grossmann, and Ph. Tchamitchian (Springer-Verlag, Berlin, 1989).
[20] B. Yang, K. J. Schafer, B. Walker, K.C. Kulander, P. Agostini, and L. F. DiMauro, Phys. Rev. Lett. **71**, 3770 (1993).
[21] G.G. Paulus, W. Nicklich, H. Xu, P. Lambropoulos, and H. Walther, Phys. Rev. Lett. **72**, 2851 (1994).
[22] G.G. Paulus, W. Nicklich, and H. Walther, Europhys. Lett. **27**, 267 (1994).
[23] X. Chen, A. Sanpera, and K. Burnett (unpublished).
[24] L.D. Landau and E.M. Lifshitz, *Quantum Mechanics* (Pergamon, Oxford, 1977).